Journal of Hazardous Materials 388 (2020) 121765

Contents lists available at ScienceDirect

Journal of Hazardous Materials

journal homepage: www.elsevier.com/locate/jhazmat

Immobilization of cesium with alkali-activated blast furnace slag

M. Komljenović[a,*], G. Tanasijević[a], N. Džunuzović[a], J.L. Provis[b]

[a] Institute for Multidisciplinary Research, University of Belgrade, Kneza Višeslava 1, 11030 Belgrade, Serbia
[b] Department of Materials Science and Engineering, University of Sheffield, Mappin St, Sheffield S1 3JD, United Kingdom

GRAPHICAL ABSTRACT

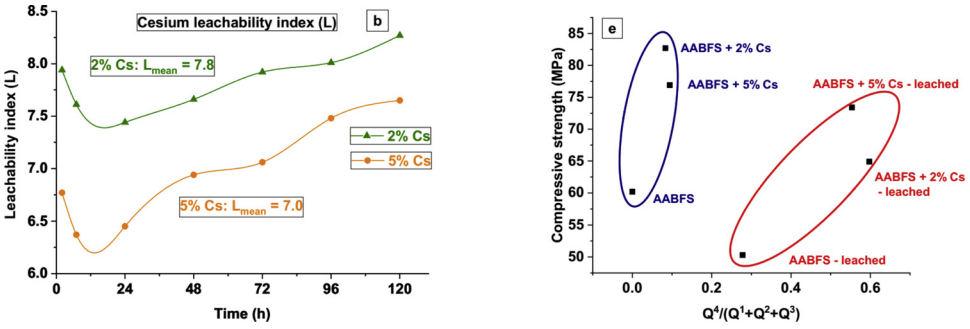

ARTICLE INFO

Editor: Daniel C.W. Tsang

Keywords:
Hazardous waste
Solidification
Alkali-activated binder
Leaching
Nanostructure

ABSTRACT

Alkali-activated binders (AABs), as a promising alternative to Portland cement, are now being used on a commercial scale in various applications around the world, including hazardous and radioactive waste immobilization. In this paper, the leaching resistance, strength, and nanostructural alteration of alkali-activated blast furnace slag (AABFS) doped with 2 % and 5 % cesium were investigated. The addition of cesium caused a significant increase in the compressive strength of AABFS, followed by mild strength reduction after leaching. AABFS can be considered a potentially efficient matrix for cesium immobilization, since the mean leachability index in both cases (2 % and 5 % of Cs added) was above the threshold value of 6. Both doping with Cs and leaching caused the transformation of the AABFS nanostructure. The majority of the aluminum that was released from the C-A-S-H gel due to leaching remained within the AABFS matrix, initiating gel reconstruction: the C-A-S-H gel was converted to C-S-H gel, and an additional N-(C)-A-S-H gel was also formed. Cesium was preferentially associated with the N-(C)-A-S-H gel rather than with the C-A-S-H gel. The results of this research seem to be in good agreement with the Cross-linked Substituted Tobermorite Model (CSTM).

1. Introduction

Immobilization of low- and intermediate-level radioactive wastes in Portland cement has been practiced for many years due to the inexpensive and readily available materials involved, and the simple and low cost processing routes. Portland cement reacts with water under ambient conditions to form a hardened and water-resistant product, with good mechanical characteristics, radiation and thermal stability, and the capability to immobilize a wide range of inorganic waste species (Glasser, 2011; Abdel Rahman et al., 2015). To improve the properties of a waste-containing matrix, particularly its resistance to leaching of radionuclides, supplementary cementitious materials such as blast furnace slag, fly ash, metakaolin, and different types of clays or zeolites are blended with Portland cement for use in waste

* Corresponding author.
E-mail address: miroslav.komljenovic@imsi.rs (M. Komljenović).

https://doi.org/10.1016/j.jhazmat.2019.121765
Received 4 October 2019; Received in revised form 24 November 2019; Accepted 27 November 2019
Available online 27 November 2019

immobilization in practice. However, the susceptibility of Portland cement-based waste-containing matrices to degradation in some aggressive environments requires further analysis, particularly in cases where the radionuclides of interest are not strongly chemically bound within the cement hydration products.

In the past several decades alkali-activated binders (AABs) have been successfully developed as a promising alternative to Portland cement, and are now being used on a commercial scale in the construction industry and in various other applications around the world (Provis and van Deventer, 2014; Pacheco-Torgal et al., 2015; Shi et al., 2019). AABs have also been frequently studied, and to some extent applied, for immobilization of hazardous, toxic and nuclear wastes, contributing significantly to the available toolkit of materials that can be applied to protect the biosphere from further contamination (Lancellotti et al., 2015; Bernal et al., 2014).

The number of studies related to the use of AABs for radioactive waste immobilization is continuously growing; low-calcium aluminosilicates such as metakaolin (Arbel Haddad et al., 2017; Lambertin et al., 2013; Kuenzel et al., 2015) and ASTM Class F fly ash (Al-Jubouri et al., 2016; Wang et al., 2019; Li et al., 2013) have been most frequently used as solid precursors for AAB synthesis. High calcium aluminosilicate material, such as blast furnace slag (BFS), was used either as a sole solid precursor or combined with other solid aluminosilicate precursors (El-Naggar et al., 2019; El-Naggar and Amin, 2018; Vandevenne et al., 2018; Kryvenko et al., 2015).

Physical and chemical properties of solid precursors, the type and concentration of alkali activator, and curing conditions (temperature, relative humidity, and time) all have key roles in determining the properties of AABs (Provis and van Deventer, 2014; Komljenović, 2015). Sodium silicate and sodium hydroxide are the most frequently used alkali activators, while potassium silicate, sodium carbonate and calcium hydroxide, sodium silicate and sodium carbonate, sodium sulfate, and simulated high-alkaline waste are less frequently used. The activator selection is also essential in ensuring adequate flow properties, and flow retention, so that the materials can be processed in a radiological environment (Steins et al., 2012).

Cesium is considered to be one of the most difficult radionuclides to immobilize in Portland cement due to its weak bonding and high mobility within many common binder matrices. Consequently, the majority of studies with AABs have focused on cesium immobilization (Arbel Haddad et al., 2017; Li et al., 2013; El-Naggar et al., 2019; El-Naggar and Amin, 2018; Vandevenne et al., 2018; Jang et al., 2016; Deng et al., 2015; Wagh et al., 2016), while strontium, cobalt, and europium were studied to a lesser extent (Kuenzel et al., 2015; Al-Jubouri et al., 2016; El-Naggar et al., 2019; Vandevenne et al., 2018; Kryvenko et al., 2015; Jang et al., 2016; Walkley et al., 2020; Tsutsumi et al., 2014; El-Naggar, 2014). The immobilization of aqueous solutions of non-radioactive isotopes or simulated radioactive wastes is performed in most experimental campaigns, since the immobilization of actual radioactive wastes brings a significant radiation hazard, and the chemistry of radioisotopes can usually be simulated with sufficient accuracy by the use of stable isotopes of the same element, where these exist.

Generally, setting time, strength, and leaching testing are considered to provide the most significant information regarding the efficiency of toxic and radioactive waste immobilization, and so are widely used to determine the influence of immobilized species on the properties of AABs. Different leach testing protocols have been applied in published studies, such as American National Standards Institute/American Nuclear Society ANSI/ANS-16.1 (Arbel Haddad et al., 2017; Jang et al., 2016; Deng et al., 2015; Wagh et al., 2016), ASTM C1285 (Wagh et al., 2016), the International Atomic Energy Agency static test proposed by Hespe (El-Naggar et al., 2019; El-Naggar, 2014), the Chinese GB7023-86 standard (Kryvenko et al., 2015), and the French National Radioactive Waste Management Agency – ANDRA standard (Cantarel et al., 2015). However, the results reported by different authors are sometimes contradictory, probably due to the different experimental conditions and testing methods applied, including the type of solid precursors used in alkali-activation, the nature and concentration of the alkali activator, curing conditions, as well as the type and concentration of the toxic material to be immobilized. It is clear that it is not always possible to directly compare the outcomes of different studies when assessing the influence of different AAB formulation parameters on the effectiveness of waste immobilization. The existence of such a variety of factors and experimental conditions that can influence AAB performance underpins the need for testing protocols specifically designed for assessing the suitability of AABs for radioactive waste immobilization. Obviously, more experimental research and data are required to fill the existing knowledge gap, particularly regarding cesium immobilization with AABs. Although ^{137}Cs is an isotope with a moderate half-life (30 years), it is a key constituent of many waste streams and so merits careful attention in the design of immobilization matrices and processes.

Since experimental research (either laboratory or field) is expensive and time consuming, other methods such as molecular dynamics simulations are also frequently used to predict immobilization mechanisms (Ma et al., 2019). Several recent studies based on molecular dynamics simulations have analyzed the interaction of cesium with C–S–H gel (Jiang et al., 2017; Duque-Redondo et al., 2018; Arayro et al., 2018), which provides insight that aids in the analysis of results obtained from experimental studies such as this. (Jiang et al., 2017) identified two types of adsorbed ions at the C–S–H surface: the strong inner-sphere adsorbed cesium ions, which are restricted to the vacancies between neighboring silicate chains, and the weak outer-sphere adsorbed cesium ions which can only be connected with bridging tetrahedra by one Cs–O bond. (Duque-Redondo et al. (2018)) identified similar types of Cs adsorption configurations on the C–S–H surface: an inner-sphere surface site where Cs is strongly bound, an outer-sphere surface site where Cs is loosely bound, and Cs free in the nanopores. They also concluded that Cs cannot displace the intrinsic Ca from the C–S–H surface. (Arayro et al. (2018)) concluded that Cs adsorption in the C–S–H interlayer is preferred to Cs adsorption at the nanopore surface when Cs concentrations are lower than 0.19 mol/kg, while the interlayer sorption decreases as the Ca/Si ratio increases.

Bearing in mind the existing knowledge gap in this field, the specific objectives of this research are: a) to use high concentrations of cesium to identify its impact on mechanical and structural properties of AABFS; b) to determine the effectiveness of cesium immobilization within BFS alkali-activated with sodium silicate solution, c) to identify any nanostructural modification of AABFS due to doping with Cs and/or leaching, and d) to determine more precisely the immobilization mechanisms involved. Therefore, setting time, leaching, and strength of alkali-activated blast furnace slag (AABFS) doped with 2 % and 5 % cesium (i.e., a solidified simulated radioactive waste), along with the multi-technique characterization of structural evolution of AABFS due to doping with Cs and leaching, were investigated. A short-term leaching procedure (up to 5 days) was performed according to the ANSI/ANS-16.1-2003standard method (ANSI/ANS-16.1, 2003).

2. Experimental

2.1. Materials

In this work, granulated blast furnace slag (BFS) from pig iron production at the facility “Železara Smederevo” (Serbia) was used as a solid precursor for the synthesis of the alkali-activated binders. Prior to the testing, granulated BFS was ground so that its specific surface area (according to the Blaine test) was ~400 m^2/kg.

The chemical composition of BFS was examined by a classical chemical analysis (alkali fusion), and the results are given in Table 1, while the particle size distribution of ground BFS was examined by wet sieving and the results are given in Table 2.

Table 1
Chemical composition of BFS.

Component	SiO_2	Al_2O_3	Fe_2O_3	MnO	CaO	MgO	SO_3	S	Na_2O	K_2O	LOI[a]
Mass (%)	39.88	6.68	0.97	0.63	39.34	8.61	0.20	0.51	0.42	0.61	1.23

[a] LOI is loss on ignition at 1000 °C.

Table 2
Particle size distribution of ground BFS.

Particle size	< 45 μm	45-63 μm	63 – 100 μm	> 100 μm
Mass (%)	85.98	6.50	4.11	3.41

Sodium silicate solution (13.60 % Na_2O, 26.25 % SiO_2, 60.15 % H_2O on a mass basis; Galenika-Magmasil, Serbia) was used as an alkali activator; its modulus (SiO_2/Na_2O mass ratio) as supplied was 1.93. The sodium silicate modulus was adjusted to 1.5 by adding sodium hydroxide pellets (98.5 % NaOH, Lach-Ner, Czech Republic), according to a previously optimized procedure (Komljenovic et al., 2010; Nikolić et al., 2015; Marjanović et al., 2015). Cesium chloride (99.5 % CsCl, Superlab, Serbia) was used as the Cs source, and was dissolved into the mixing water of doped samples.

2.2. Paste preparation

The AABFS pastes were prepared by mixing ground granulated BFS, sodium silicate solution, and water or cesium chloride solution (in the case of AABFS doped with Cs). The dose of Na_2O was 4 % in all cases, and the doping level of Cs was either 2.0 % or 5.0 %, where these percentages are defined with respect to the total mass of BFS. Previous investigations (Vandevenne et al., 2018; Nikolić et al., 2018) confirmed that relatively high concentrations of toxic elements are required for more precise analysis of the processes involved. The mix proportions of AABFS pastes, as well as their setting times according to EN 196–3 (EN 196-3, 2008) and flow diameters according to EN 1015-3 (EN 1015-3, 2008) are given in Table 3. The water content used in defining the water/binder (w/b) ratio was calculated as the sum of the water from sodium silicate solution and the water added for appropriate consistency, while binder was defined as the sum of BFS, the solid part of the activator, and any added CsCl. The AABFS paste was mixed for two minutes, then poured into a cylindrical plastic mold (ø 60 × 10 mm), after which the air bubbles were removed using a vibrating table. The AABFS pastes were cured covered with plastic for 24 h at 95 °C, and then, also covered, at room temperature until testing, according to a previously optimized procedure (Nikolić et al., 2015; Marjanović et al., 2015).

2.2.1. Paste preparation for structural testing

For the investigation of microstructural characteristics of AABFS by XRD, NMR and FTIR methods, fragments of paste samples were roughly crushed and then dry-pulverized for 15 min in a laboratory agate mill (Netzsch Pulverisette). Pulverizing in the agate mill was carried on for additional 45 min in isopropyl alcohol to stop the reaction process of alkali activation. After being pulverized, the samples were dried in a laboratory oven at 50 °C for 2 h.

For SEM/EDS analysis, selected fragments of the AABFS paste samples were immersed in isopropyl alcohol for 24 h and and then dried at 50 °C for 2 h. Then the samples were ground and polished using successively finer silicon carbide (SiC) grinding papers (360, 600, 800, 1200 and 2000 grit) for approximately 5 – 30 min (longer polishing with finer papers), with acetone as a lubricant. After polishing, the samples were rinsed in acetone in an ultrasonic bath for 3 min and finally dried in a laboratory oven at 50 °C for 2 h. Prior to SEM/EDS analysis the samples were Au-coated.

2.3. Mortar preparation

Mortars of AABFS were prepared by adding the activator solution of specified concentration to water (containing CsCl for doped samples) and then mixing this solution with the BFS and standard sand (BFS:sand ratio was 1:3) following as closely as possible the procedure of EN 196–1 (EN 196-1, 2008). The dose of activator was 4 % Na_2O by mass of BFS, while the concentration of Cs was either 2.0 % or 5.0 % with respect to the total mass of BFS. The amount of water required to obtain similar workability for each mortar sample was determined by the flow table test according to EN 1015-3 (EN 1015-3, 2008); the target mortar flow was 120 ± 5 mm. Water/binder ratios are defined as described above for the paste samples. Mortars were homogenized in an automatic mixer for 3 min and cast into triplicate mortar prisms (40 × 40 × 160 mm) on a vibrating table. The mix proportions of the AABFS mortars are given in Table 4. The AABFS mortars were cured under the same conditions as the AABFS pastes.

2.4. Methods of characterization

2.4.1. Leaching tests

Leaching of different elements (Si, Al, Ca, Mg, Na, K, Fe, and Cs) from hardened AABFS pastes was determined according to the ANSI/ANS-16.1-2003standard procedure. This test is a semi-dynamic leach experiment that consists of submerging a monolithic sample, with a fixed geometry, into water at a fixed liquid-volume to solid-geometric surface area ratio, and replacing all of the leachate at given time intervals. The leachates are then analyzed for key constituents.

Demineralized water (< 5 μS/cm at 25 °C) was used as a leachant at a liquid volume to waste-form surface area (L/S) ratio of 10 ± 0.2 cm. The specimens were put in a plastic container with the leachant, supported by a grid plastic holder that does not exclude more than a small fraction of the external surface of the specimen from exposure to the leachant. The standard leaching test was performed without any stirring within a period of 5 days, where the leachate was completely replaced by fresh leachant after cumulative leach times of 2, 7, 24, 48, 72,

Table 3
AABFS paste composition and setting time.

Sample	BFS mass (g)	Sodium silicate mass (g)	Added water (g)	CsCl mass (g)	Flow (mm)	Water/ binder ratio	Setting time (min)	
		4 % Na_2O					Initial	Final
AABFS	450	108.1	40	0	204	0.21	15	30
AABFS + 2 % Cs	675	162.15	60	17.1	249	0.21	40	60
AABFS + 5 % Cs	675	162.15	60	42.75	264	0.20	60	80

Table 4
AABFS mortar composition.

Sample	BFS mass (g)	Standard sand mass (g)	Sodium silicate mass (g) 4 % Na_2O	Water added (g)	CsCl mass (g)	Flow (mm)	Water/binder ratio	Mortar average density (g/cm^3)
AABFS	450	1350	108.1	130	0.00	125	0.35	2.21
AABFS + 2 % Cs	450	1350	108.1	110	11.4	124	0.34	2.28
AABFS + 5 % Cs	450	1350	108.1	100	28.5	115	0.33	2.25

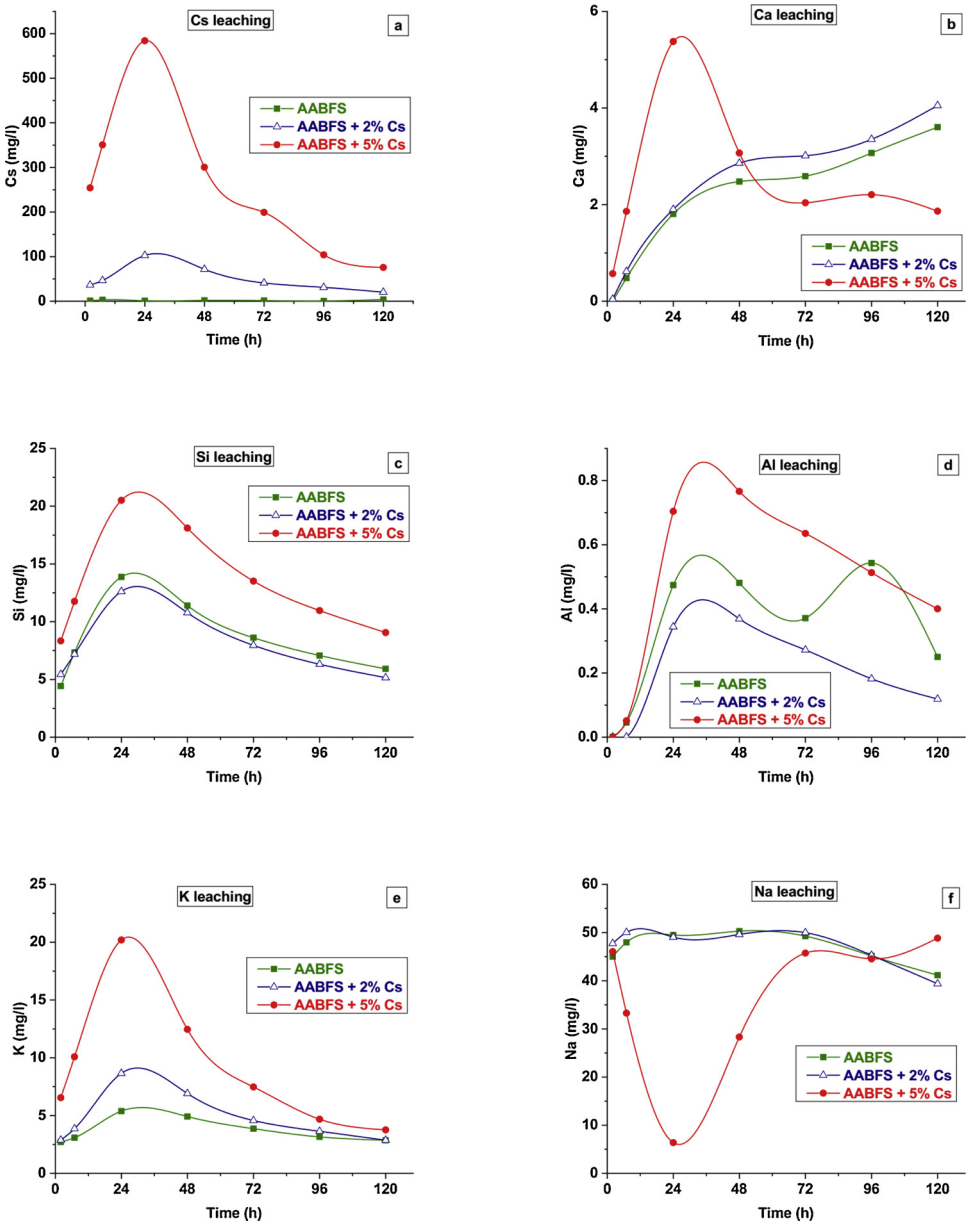

Fig. 1. Incremental leaching of main elements from the AABFS matrices up to 120 h of testing, with and without Cs added. (Analytical uncertainty in each point is approximately 1 %).

96, and 120 h. Each collected leachate was vacuum filtered through a 0.45 µm membrane filter, after which its pH was measured with a pH meter (HANNA instruments HI 991001, USA).

An inductively coupled plasma optical emission spectrometer (ICP–OES, Spectro–Genesis EOP II, Spectro Analytical Instruments GmbH, Kleve, Germany) was used to determine the concentrations of leached elements present in the leachate. Before testing, the leachate was acidified with nitric acid (65 % HNO_3, Analar Normapur, EC) to a pH value less than 2 to ensure that it remained stable until being subjected to instrumental analysis.

2.4.2. *Mortar strength*

The strengths of all AABFS mortars were determined according to EN 196–1 (EN 196-1, 2008), using a Compression testing machine (Matest).

2.4.3. XRD analysis

The mineralogical composition of alkali-activated BFS was determined by XRD analysis, using a SmartLab X-ray diffractometer (Rigaku) with Cu Kα radiation (λ = 0.1542 nm), operating at 40 kV and 30 mA. The data were collected from 5 - 80° 2θ with a step size of 0.05° and an exposure time of 3 s per step. For the identification of crystalline phases the "PCPDFWIN" and "Crystallographica Search Match" software (based on JCPDS-ICDD database) were used.

2.4.4. ATR-FTIR analysis

The FTIR spectra were collected using a Perkin Elmer Spectrum Two FT-IR spectrometer in attenuated total reflectance mode, from 4000 – 400 cm^{-1}, at a resolution of 4 cm^{-1} and collecting 4 scans per spectrum.

2.4.5. SEM/EDS analysis

SEM analysis was carried out using a VEGA TS 5130 MM Tescan electron microscope, coupled with an INCAPentaFET-x3 (Oxford Instruments) detector for EDS analysis. SEM imaging of the sample surface was performed at an accelerating voltage of 20 kV, while EDS analysis used an accelerating voltage of 10 kV, with no less than 50 acquisitions per sample. During the EDS analysis, it was taken care that the visible site of interest should not include unreacted BFS particles.

2.4.6. ^{29}Si MAS NMR analysis

^{29}Si MAS NMR spectra of AABFS were obtained at a Larmor frequency of 79.49 MHz using a Bruker MSL 400 system and upgraded Apollo console (Tecmag), pulse angle π/2, pulse time 4 μs, recycle delay 30 s, for a total recording time of 500 min per sample, and a rotation rate of 5 kHz. Chemical shifts $\delta(^{29}Si)$ were externally referenced to 2.2-dimethyl-2-silapentane-5-sulfonate (DSS) as a standard. Prior to the ^{29}Si MAS NMR analysis the iron content was minimized by exposing the AABFS samples to a strong magnetic field (Nikolić et al., 2018). Deconvolution of the overlapping resonance peaks in the spectra of AABFS was carried out using the OriginPro software, whereby Gaussian functions, constant peak widths and locations were used throughout the whole process, and analyzed to represent a tobermorite-like C-A-S-H structure in accordance with the "Cross-linked Substituted Tobermorite Model" (CSTM) (Myers et al., 2013; Walkley and Provis, 2019).

3. Results and discussion

3.1. Leaching

3.1.1. Composition and pH of leachate

The incremental and cumulative leach fractions of Cs, the AABFS matrix main building blocks (Ca, Si, and Al), as well as alkali cations (Na and K) present in the leachate over the period of 120 h are given in Figs. 1 and 2, repectively. The concentrations of Mg and Fe present in the leachate were below the detection limit throughout the whole period of testing, and therefore are not shown.

The concentration of Cs leached from AABFS has reached its peak after the first 24 h of testing in the case of AABFS doped with both 2 % Cs and 5 % Cs (Fig. 1a). Similar leaching patterns were also present in the case of other elements tested (Fig. 1b-e). The fast increase of Cs, Ca, Si, Al, and K concentrations after the first 24 h of testing was probably due to the leaching of non-bound or loosely bound ions present in the pore solution at or close to the surface of specimens, which is also known as the surface wash-off phenomenon (Abdel Rahman and Zaki, 2009). Between 48 and 120 h of testing the leaching rates were significantly lower due to the diffusion controlled migration of ions through the AABFS matrix. While developing models for predicting the long-term behavior of the immobilized waste from matrices, the surface wash-off phenomenon should be taken into account.

Besides these similarities, there are also some (important) noticeable differences in leaching patterns. The presence of 2 % Cs did not significantly influence the leaching of Ca, Si, or Na, while some minor influence was noticed in the case of K and Al. However, the presence of 5 % Cs in the AABFS matrix had a profound impact on leaching patterns of other elements tested: the leaching of Ca, Si, Al and K was promoted (Fig. 1b-e), while the leaching of Na was inhibited, particularly in the first 24 h (Fig. 1f). The overall concentration of aluminum present in the leachate was very low, which is in agreement with our previous findings (Komljenović et al., 2012). Given that it is relatively difficult to remove Si from C–A–S–H gel by aqueous leaching (Vandevenne et al., 2018), the relatively high concentration of silicon present in the leachate is probably related to the excess of activator (sodium silicate) present in the pore solution of the AABFS matrix.

The leaching results suggest that while cesium was released at quite a high concentration, there was some competition between the other alkali metals (potassium and sodium) during leaching. The concentration of potassium in the leachate reached its maximum after the first 24 h of testing, while the concentration of sodium in the leachate reached its minimum at the same time (clearly visible in the case of 5 % Cs, Fig. 1f). In the following period the concentration of potassium in the leachate started to decrease while the concentration of sodium started to increase. The differences in the leaching patterns of alkali metal cations (cesium, potassium and sodium) were probably a consequence of their different ionic radii and bonding strength within the AABFS matrix. A similar phenomenon has previously been described as being related to the Hofmeister effect in electrolyte solutions and in cation adsorption at different surfaces (Salis and Ninham, 2014). These findings are also in agreement with molecular dynamics simulations which concluded that the adsorption capacity of monovalent cations on the C–S–H surface increases with decreasing ionic radius, in the sequence $Na^+ > > K^+ > Cs^+$ (Jiang et al., 2017). The Na^+ ions, due to their smaller hydration shell and stronger Na^+–O_s connections, possess a higher ability to penetrate into the surface cavities and thus reside in the silicate channel for a longer time than the Cs^+ and K^+ ions.

Obviously, AABFS is unable to host large amounts of alkali ions in the gel structure, having a major portion of highly mobile alkalis present in the pore solution of the AABFS matrix (Myers et al., 2017), which can readily migrate to the leachant during leach testing.

Cumulative leach fractions of the main elements leached from the AABFS matrices up to 120 h are given in Fig. 2, confirming the relatively high mobility of alkali cations (particularly Cs) in the pore system, and the high degree of their leaching from AABFS matrices.

The concentration of sodium present in the leachate was relatively high throughout the whole period of testing (Fig. 2f), but a lower concentration of sodium was noticeable when AABFS was doped with 5 % Cs. These results suggest that the higher concentration of Cs had a positive impact on the resistance of AABFS matrix to aqueous leaching of Na, even though the total content of alkali cations in the matrix was higher. It is possible that there is some influence from the chloride that accompanied the Cs cations, but this has not yet been tested in detail.

It is well-known that if the leaching process is diffusion-controlled, the cumulative release of element of interest is expected to be proportional to the square root of time. The results given in Fig. 3 confirmed that the cesium release exhibited linearity with respect to the square root of time, which appears to be in accordance with Fick's Law for diffusion control. However, the slope of the lines changes after the initial 24 h of leach testing, which means that the surface wash-off was dominant phenomenon in the initial period, while the process of leaching is likely to have been diffusion controlled in the later period.

The differences in the alkali cation leaching results in the observed testing period did not have a significant impact on the pH values of the leachate (Fig. 4), regardless of the concentration of Cs cations present. The concentration of potassium was always relatively low, since potassium orriginated only from the slag (as a very minor constituent, Table 1) and not from the alkali activator. An increase in the pH of the leachate occured within the first 24 h, during which time the majority of cesium and potassium leached from the AABFS matrix, then the pH

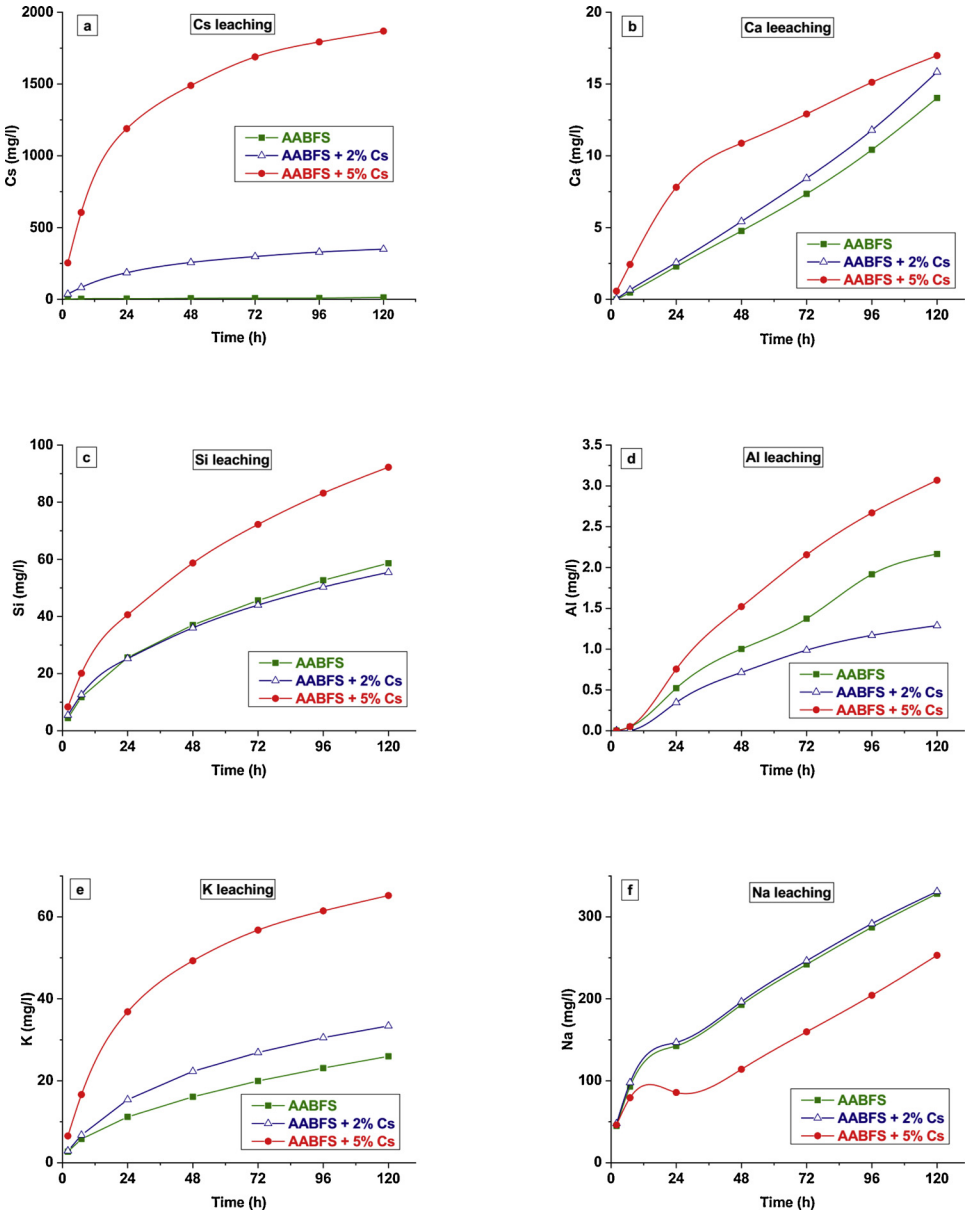

Fig. 2. Cumulative leaching of main elements from the AABFS matrices up to 120 h of testing, with and without Cs added. (Analytical uncertainty in each point is approximately 1 %).

values started to gradually decline. These results are also in good agreement with other recent findings (Vandevenne et al., 2018).

The concentration of Ca in the leachate increased over time, although always at a relatively low level and rate. Such an increase of calcium concentration might be the result of either additional dissolution of unreacted BFS grains due to the high pH of the leachate, and/or decalcification of the C-A-S-H gel. The decalcification of C-A-S-H gel might represent some threat to the structural stability of AABFS, but

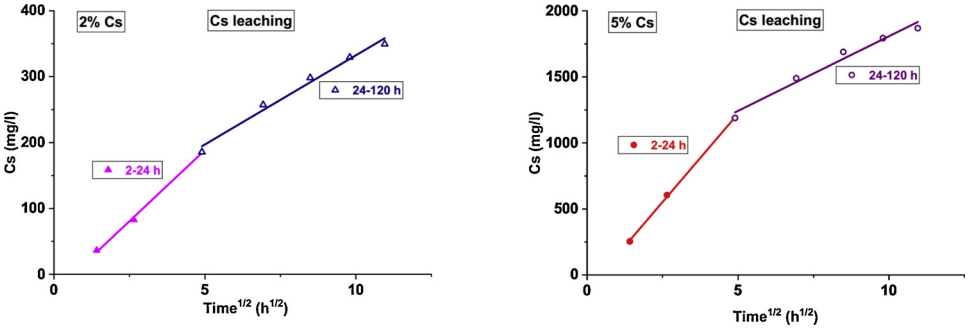

Fig. 3. Linear regression analysis of cesium leaching from the AABFS matrices doped with cesium: a) 2 % Cs and b) 5 % Cs.

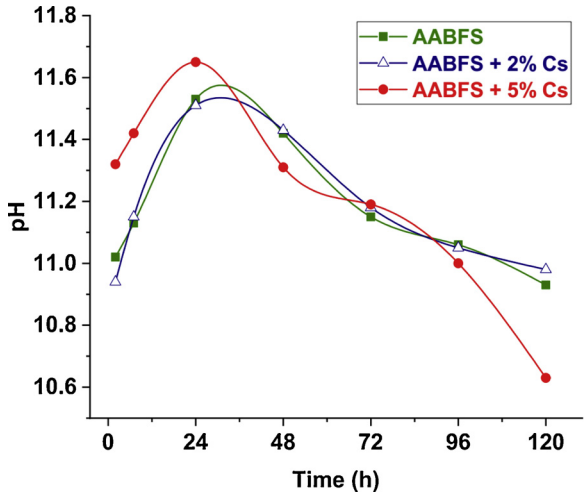

Fig. 4. pH values of leachates, up to 120 h of testing.

probably to a limited extent (Komljenović et al., 2012).

3.1.2. Diffusion coefficient (D) and leachability index (L)

The diffusion coefficient (D) and non-dimensional leachability index (L) of cesium leached from AABFS can be calculated according to the following equations (ANSI/ANS-16.1, 2003):

$$D = \pi\,[(a_n/A_o)/(\Delta t)_n]^2\cdot[V/S]^2\cdot T \quad (1)$$

where D is the effective diffusivity (cm^2/s), a_n is the quantity of cesium released from the specimen during leaching interval n (g), A_o is the total quantity of cesium in the specimen at the beginning of the first leaching interval (g), $(\Delta t)_n = t_n - t_{n-1}$ is the duration of the n^{th} leaching interval (s), V is the volume of the specimen (cm^3), S is the geometric surface area of the specimen in contact with the leachant as calculated from its measured dimensions (cm^2), and T is the leaching time (s) representing the "mean time" of the leaching interval by its quadratic mean:

$$T = [1/2(t_n^{1/2} + t_{n-1}^{1/2})]^2 \quad (2)$$

The non-dimensional leachability index (L) is defined by:

$$L_i = 1/7 \sum_{n=1}^{7} [\log(\beta/D_i)]_n \quad (3)$$

where β is a defined constant (1.0 cm^2/s).

Based on the results of cesium leaching tests (given in Fig. 1a) and Eqs. (1), (2), and (3), the diffusion coefficient (D) and leachability index (L) of cesium leaching from AABFS doped with 2 % and 5 % Cs were calculated, Fig. 5.

The leachability index (L) is a parameter that characterizes the leaching resistance of an element of interest, and can be used to estimate the applicability of a certain material or matrix for safe immobilization of hazardous waste. An L value of 6 is considered as the threshold for a given matrix to be accepted as adequate for the immobilization of radioactive wastes (Abdel Rahman et al., 2007). From the results presented here, the mean leachability index of cesium leached from alkali-activated BFS doped with 2 % and 5 % Cs (7.8 and 7.0, respectively, Fig. 5b) exceeded the minimum required value of 6. The results presented here are comparable with the results for cesium immobilized in Portland cement matrices obtained under the same experimental conditions (ANSI/ANS-16.1), where after 5 days of leaching the mean cesium diffusion coefficient and leachability index were $1.2{\cdot}10^{-7}$ cm^2/s and 7.0, respectively (Jang et al., 2016). Consequently, an AABFS synthesized under the experimental conditions used in this study can be considered as a potentially efficient matrix for immobilizing cesium from radioactive wastes, comparable to conventional Portland cement in terms of leaching resistance.

It also seems resonable to expect that by the addition of some other material with high sorption capacity, such as clay or zeolite, the leachability index of cesium immobilized in alkali-activated BFS might be additionally improved (Bernal et al., 2014), but such work is beyond the scope of the current study.

3.2. Strength of AABFS mortars before and after leaching

The results of AABFS mortar compressive strength testing are given in Table 5. The AABFS mortar reference samples achieved compressive strengths of ~60 MPa after 24 h of reaction at 95 °C. Doping AABFS with 2 % or 5 % Cs resulted in a ~20 MPa increase in mortar compressive strength, probably due to promotion of the dissolution of BFS or some structural reorganization of AABFS gels. The causes of these outcomes will be analyzed in detail in the following sections.

After 5-day leaching tests all AABFS mortar samples suffered some loss of strength; the smallest strength loss was observed with addition of 5 % Cs, suggesting that the higher concentration of Cs present in the AABFS matrix had a positive effect on the structural stability of the AABFS matrix. Despite the loss of strength after 5 days of leaching, AABFS mortars doped with both 2 % and 5 % Cs had higher compressive strengths than the reference AABFS mortar.

It is reasonable to assume that the decalcification of C-A-S-H gel due to the impact of deionized water occurred to some extent (Komljenović et al., 2012). However, the strength variation of AABFS mortar as a result of 5 days of leaching cannot be fully explained by the calcium leaching, since the total amount of this element leached is more or less similar in all cases (Fig. 2b). The 5 % addition of cesium to the AABFS matrix must have either suppressed calcium leaching (i.e. increased the resistance of the C-A-S-H gel to leaching) or promoted further dissolution of unreacted BFS grains and thus continuation of alkali activation, since in this case the smallest (5 %) loss of strength was observed.

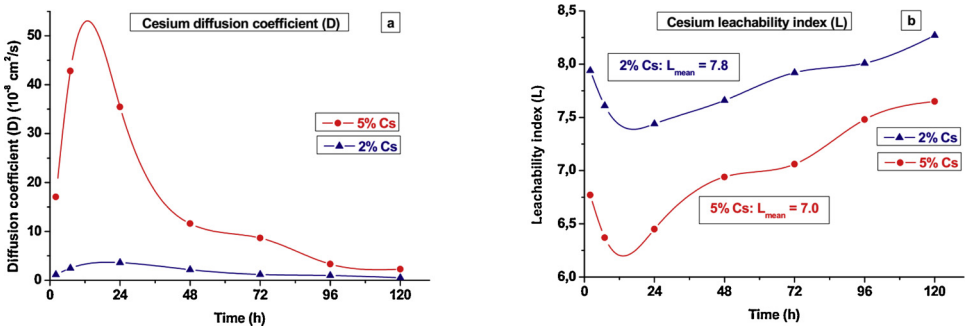

Fig. 5. Diffusion coefficient (a) and non-dimensional leachability index (b) of cesium leached from the AABFS matrices doped with 2 % Cs and 5 % Cs versus time.

Table 5
Compressive strength of AABFS mortars (with and without Cs added; before and after leaching).

Sample type	AABFS – ref.	AABFS + 2 % Cs	AABFS + 5 % Cs
	Compressive strength and standard deviations (MPa)		
Initial (before leaching)	60.2 ± 1.9	82.8 ± 2.9	76.9 ± 1.8
After 5-day leaching	50.4 ± 2.5	64.9 ± 1.4	73.4 ± 2.2
	Relative compressive strength *(with respect to the non-leached reference AABFS)*		
Initial (before leaching)	1.00	1.38	1.28
After 5-day leaching	0.84	1.08	1.22
	Relative compressive strength *(with respect to its non-leached counterpart)*		
Initial (before leaching)	1.00	1.00	1.00
After 5-day leaching	0.84	0.78	0.95

3.3. XRD analysis

XRD patterns of AABFS with and without addition of Cs, as well as before and after leaching, are given in Fig. 6.

The main product of alkali-activation of BFS was poorly-crystalline calcium aluminosilicate hydrate C-A–S–H, while the other two major crystalline phases identified in AABFS were melilite ($Ca_2(Mg_{0.5}Al_{0.5})(Si_{1.5}Al_{0.5}O_7)$; JCPDS #79-2423) and merwinite ($Ca_3Mg(SiO_4)_2$; JCPDS #89-2432), which originated from the initial BFS. Detailed XRD analysis of the initial BFS used in this study is given elsewhere (Komljenović et al., 2012).

The presence of secondary calcite ($CaCO_3$; JCPDS #47-1743) and trona ($Na_3H(CO_3)_2(H_2O)_2$; JCPDS #78-1064), formed as a result of carbonation during AABFS curing and sample preparation for this analysis, was also tentatively identified, although their major peaks overlapped with peaks attributed to other crystalline phases.

Recrystallization of cesium chloride was not identified in any case, but a new phase was formed when AABFS was doped with 5 % Cs. This newly formed phase might be a cesium-containing aluminosilicate phase, such as $Cs_2Al(OH)(SiO_4)_2$ (JCPDS #37-0063) as indicated in Fig. 6. However, this identification cannot be considered definitive since it is based only on a small single peak located at 31.7° 2θ. No crystalline hydrotalcite-like phases, which are often present in AABFS binders, were identified here by XRD. Hydrotalcite can be formed in AABFS when the initial BFS contains sufficient quantity of Mg. However, hydrotalcite or hydrotalcite-like phases can also be intimately intermixed into the C-S-H structure and thus not identifiable by XRD analysis, which is in agreement with our previous findings when the same type of BFS was used (Komljenović et al., 2012).

The only identifiable change as a result of the leaching is the disappearance of the newly formed cesium-containing aluminosilicate phase. Obviously, this new phase was highly soluble in water since it disappeared completely after leaching.

3.4. ATR-FTIR analysis

FTIR spectra of BFS, and AABFS with and without addition of Cs before and after leaching, are given in Fig. 7. All of the FTIR spectra show a characteristic broad and asymmetric peak located between 800 and 1250 cm^{-1}, with the maximum located at ~940 cm^{-1}.

Beside this major peak, some other peaks present in the initial BFS were also identified: a broad peak located at 1486 cm^{-1} together with a shoulder located at 1420 cm^{-1} which can be assigned to the asymmetric stretching vibration of carbonate phases, and a sharp peak located at 856 cm^{-1} which can be assigned to the out of plane bending vibration of carbonates (Nedeljkovic et al., 2018; Bernal et al., 2010; Palacios and

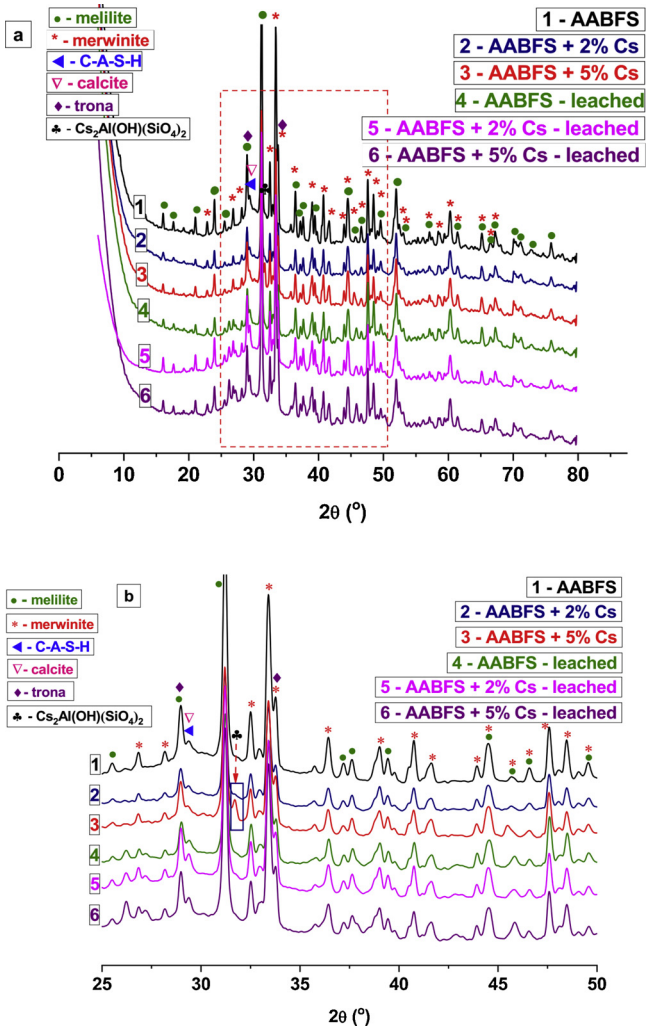

Fig. 6. XRD patterns of AABFS with and without Cs added; before and after leaching: (a) full patterns; (b) expansion of region marked by the red box in (a) (For interpretation of the references to colour in this figure legend, the reader is referred to the web version of this article).

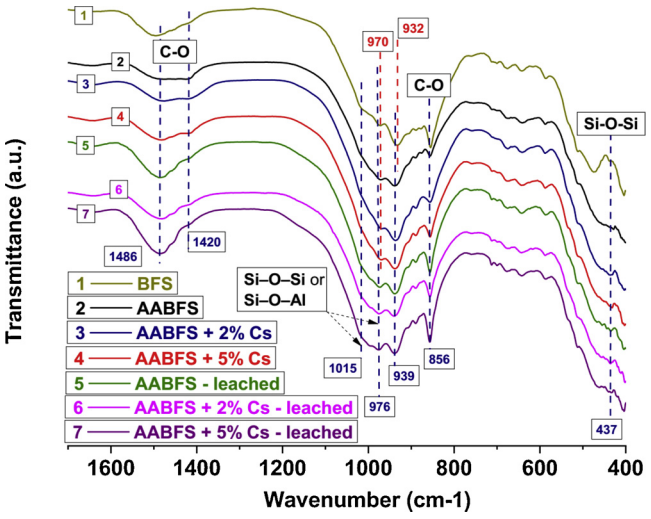

Fig. 7. FTIR spectra of BFS and AABFS (with and without Cs added; before and after leaching).

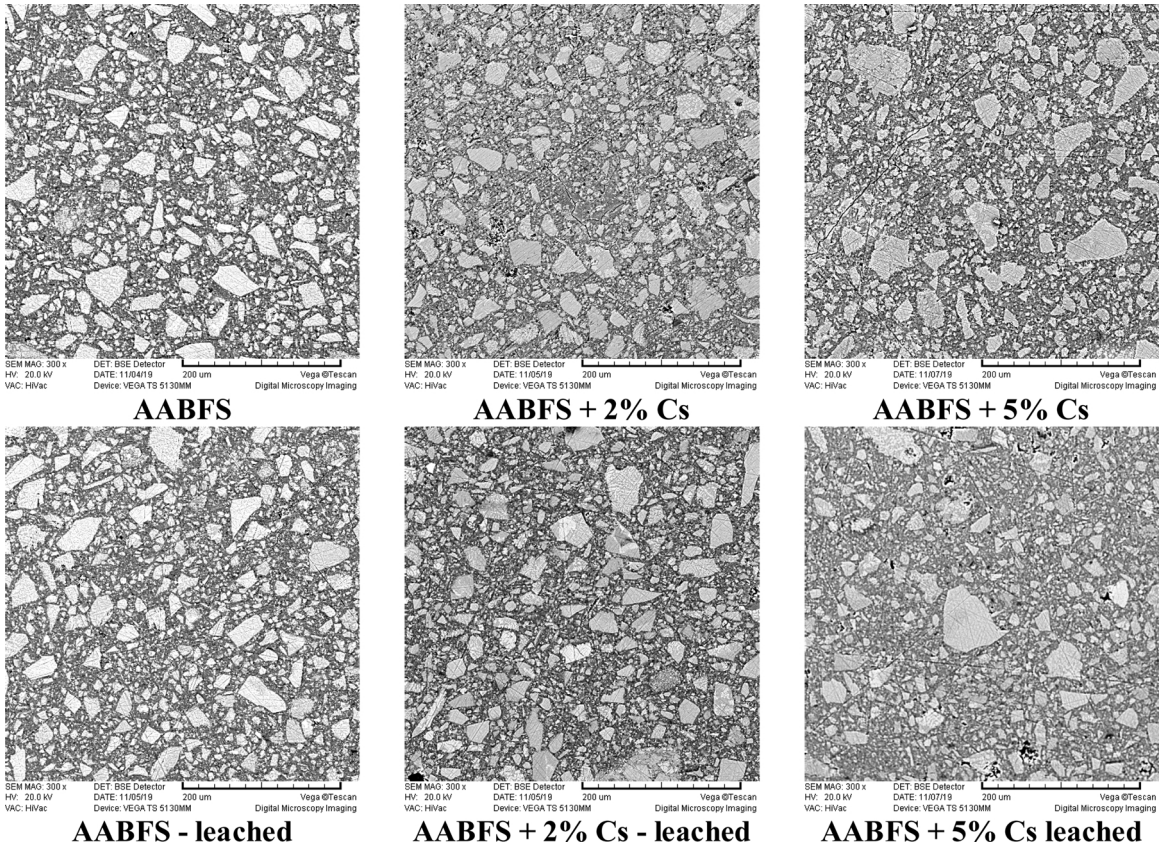

Fig. 8. SEM images of AABFS (with and without Cs added; before and after leaching).

Puertas, 2011).

It is well-known that the insertion of tetrahedral Al can transform a layered C–S–H structure into a cross-linking branched structure by polymerizing with the defective silicate chains (Myers et al., 2015). The most visible effect of alkali activation of BFS was an increase in the intensity of the peak located at 976 cm^{-1}. This peak can be assigned to the asymmetric stretching vibrations of the Si–O–T (T = tetrahedral Si or Al) bonds, both within the initial anhydrous slag and the reaction products, as this frequency is characteristic of the silicon tetrahedra (SiO_4^{4-}) present in the chain structure of C–S–H or C-A-S-H gel (Bernal et al., 2010; Palacios and Puertas, 2011; García Lodeiro et al., 2008). An increase in the intensity of the peak located at 437 cm^{-1}, which can be assigned to the deformation vibrations of Si-O-Si bonds (Palomo et al., 1999), confirmed the effects of alkali activation. At the same time an increase in the intensity of carbonate peak located at 1420 cm^{-1} can be noticed, most probably as a result of formation of a new hydrated carbonate phase such as trona. The presence of this new phase was partially confirmed by XRD analysis (Fig. 6).

The doping of AABFS with Cs, particularly with 5 % Cs, caused a noticeable increase in the intensity of carbonate peaks located at 1486 and 856 cm^{-1}, meaning that doping with Cs promoted the process of AABFS carbonation. The carbonation of AABFS occurs directly in the C–A–S–H gel due to the absence of portlandite, forming an alumina-containing siliceous gel and calcium carbonate instead (Palacios and Puertas, 2006). Carbonation can also induce a loss of strength. However, doping of AABFS with Cs caused an increase in strength, rather than loss of strength. Furthermore, the peak located at 856 cm^{-1} can also be assigned to the Si–O terminal bonds in N–A–S–H gel (García Lodeiro et al., 2008), which might mean that doping of AABFS with Cs also triggered the formation of an N–A–S–H gel.

The attack of water molecules during leaching is the main cause of bond breakage. As a result of this hydrolytic reaction, the Al-O-Si bonds present in the cross-linked C-A-S-H gel will start to break, and Al − OH and Si − OH will be formed instead. Such bond breakage will lead to some degree of gel nanostructural transformation, and the possible formation of additional N-A-S-H gel. This identification is supported, at least partially, by an increase in the intensity of the peak located at 856 cm^{-1} after leaching.

A shift of the asymmetric stretching peak position of silicates to a higher wavenumber is typically connected with a lower Ca/Si ratio in the C–S–H gel or lower Al/Si ratio in the C-A-S-H or N-A-S-H gels (García Lodeiro et al., 2008; Palacios and Puertas, 2006). After leaching the peak located at 932 cm^{-1} shifted to 939 cm^{-1} and the peak located at 970 cm^{-1} shifted to 976 cm^{-1}, which suggests that a more polymerized gel structure was formed as a result of deionized water attack. Furthermore, a shoulder located at 1015 cm^{-1}, which can also be assigned to the asymmetric stretching mode of the Si–O–T (T = tetrahedral Si or Al) bonds, became more pronounced. This was probably a result of additional silicate polymerization and generations of a more silica-rich (i.e., aluminum- and calcium-poor) gel, confirming the gel nanostructure transformation due to the leaching. Because FTIR spectroscopy detects bond vibrations rather than the actual nuclei, the identification of this “silica-rich” character in the gels is related to the contributions of connectivity at each Si site to the gel bonding network, rather than the bulk composition (Provis et al., 2015).

The increased intensity of CO_3^{2-} bonds present in the case of AABFS doped with Cs, and particularly after leaching (peaks located at 1486 and 1420 cm^{-1}), indicates that these samples were more prone to carbonation in respect of the initial AABFS, as was reported previously (Bernal et al., 2010; García Lodeiro et al., 2009). However, all AABFS paste samples were ground prior to the FTIR testing and consequently the level of carbonation of AABFS was significantly increased when compared with monolithic samples (Nedeljkovic et al., 2018). Furthermore, the increased carbonation probably did not have a significant effect on leaching since it occurred mostly during sample preparation (extensive milling and drying in air) for this analysis, i.e. after the

Table 6
Atomic ratios of major elements present in AABFS as determined by SEM/EDS (with and without Cs added; before and after leaching).

	Ca/Si	Ca/Al	Al/Si
AABFS	0.59 ± (0.08)[a]	4.01 ± (0.62)	0.15 ± (0.01)
AABFS + 2 % Cs	0.61 ± (0.06)	4.06 ± (0.70)	0.16 ± (0.02)
AABFS + 5 % Cs	0.70 ± (0.14)	4.51 ± (0.82)	0.16 ± (0.03)
AABFS - leached	0.56 ± (0.06)	3.75 ± (0.55)	0.16 ± (0.02)
AABFS + 2 % Cs - leached	0.64 ± (0.09)	4.15 ± (0.74)	0.16 ± (0.01)
AABFS + 5 % Cs - leached	0.65 ± (0.12)	4.46 ± (0.88)	0.15 ± (0.02)

[a] Standard deviations, among no less than 50 replicate determinations, are given in parentheses.

leaching tests.

Structural transformation of the C-A-S-H gel in the presence of Cs may be a result of both increased carbonation and alkali-induced modification of the initial C–A–S–H gel, which promoted silicate polymerization and generated more silica-rich gel and Ca-containing N–A-S–H gel. Both processes were obviously more pronounced after leaching.

3.5. SEM/EDS analysis

The results of SEM/EDS analysis of AABFS with and without Cs added, and before and after leaching, are given in Fig. 8 and Table 6. Doping AABFS with Cs led to an increase in Ca/Si and Ca/Al atomic ratios, while the Al/Si atomic ratio remained almost constant.

There was a good correlation between Ca/Si or Ca/Al atomic ratio and compressive strength (Fig. 9), suggesting that an increase of these ratios was linked to the compressive strength increase when AABFS was doped with Cs. AABFS had an initial Ca/Si ratio of 0.59 and when AABFS was doped with Cs this ratio shifted to higher values, probably as a result of the omission of bridging tetrahedra and shortening of silica chains present in the C-A-S-H gel, or variations in the contents of interlayer Ca and of cations attached to the Si–O^- groups (Chen et al., 2004).

On the other hand, it was reported recently that adding cesium caused a decrease in the Ca^{2+} content in the AABFS matrix, when BFS was alkali activated with sodium hydroxide and the reaction took place at room temperature for 28 days (Vandevenne et al., 2018). Such a discrepancy might be the result not only of different physical and chemical properties of the BFS sources used in the two studies, but also of the experimental conditions applied in these two studies. As was explained above, sodium silicate solution was used as an alkali activator in this study and the reaction took place at elevated temperature, and both of these factors can increase BFS dissolution and the rate of reaction of alkali activation. Furthermore, a decrease in Ca/Si or Ca/Al atomic ratio due to leaching was responsible for the compressive strength decrease, since calcium leaching (Figs. 1b and 2 b) and consequent decalcification of the C-A-S-H gel present in AABFS can lead to a strength decrease (Komljenović et al., 2012).

The distribution of Cs in relation to the major constituent elements of the C-A-S-H gel (when AABFS was doped with 2 % and 5 % Cs; before and after leaching) is given in Figs. 10 and 11, respectively.

In the case of AABFS doped with 2 % Cs it is obvious that a higher concentration of cesium was associated with a lower concentration of calcium (Fig. 10a) and a higher concentration of silicon and aluminum (Fig. 10b and c). This might mean that some other type of gel, such as an aluminosilicate (N-A-S-H type) gel, was also present in the AABFS, whereby cesium was preferably associated with this gel rather than with calcium aluminosilicate gel (C-A-S-H). A similar cesium distribution was noticed after leaching (Fig. 10b, d, and f), indicating that the amount of cesium found in the leachate was probably a result of the leaching of non-bound cesium present in the pore solution of the AABFS matrix.

A higher concentration of cesium was also associated with a lower concentration of calcium in the case of AABFS doped with 5 % Cs (Fig. 11a), confirming that cesium was preferably located in the aluminosilicate gel rather than in the calcium silicate-type gel. Also, a more heterogeneous structure than in the case of AABFS doped with 2 % Cs can be noticed in Fig. 11c and e, which may be related to the somewhat lower strength of AABFS mortar (Table 5). A similar cesium distribution (with respect to calcium) was also noticed after leaching (Fig. 11b). On the other hand, after leaching the cesium distribution with respect to silicon and aluminum was more straightforward (Fig. 11d and f), indicating that leaching promoted structural reorganization of the gels present, and led to a more clearly organized structure and minor loss of strength.

3.6. Solid-state ^{29}Si MAS-NMR analysis

The ^{29}Si MAS-NMR spectra of the initial BFS and all hardened AABFS pastes (with and without Cs added, before and after leaching) are presented in Fig. 12. The deconvoluted curves are graphically depicted in Figs. 13 and 14, while the relative distributions of Q^n(mAl) sites (based on the deconvolution) are given in Table 7. The deconvolution of ^{29}Si MAS-NMR spectra was performed using the OriginPro software, with Gaussian peak shapes. The typical chemical shift of each Q^n(mAl) site was positioned according to the literature with interpretation via the Cross-Linked Substituted Tobermorite Model (CSTM) (Myers et al., 2013), since the spectra did not show clearly differentiated peaks. It was also assumed that the original position and the full width at half maximum (FWHM) of the initial BFS peaks (Fig. 13) would remain the same after alkali-activation, and only the intensities of these peaks would be reduced as a result of the reaction. Finally, the FWHM of each deconvoluted curve for Q^n(mAl) sites given in Fig. 14, other than those of the initial BFS, was limited to below 10 ppm (Bernal et al., 2013).

Based on the relative distribution of Q^n(mAl) sites (Table 7) and Eqs. (4) and (5) (Myers et al., 2013; Walkley and Provis, 2019), the mean chain length (MCL) and Al^{IV}/Si ratio of the cross-linked C-A-S-H gel structures can be calculated.

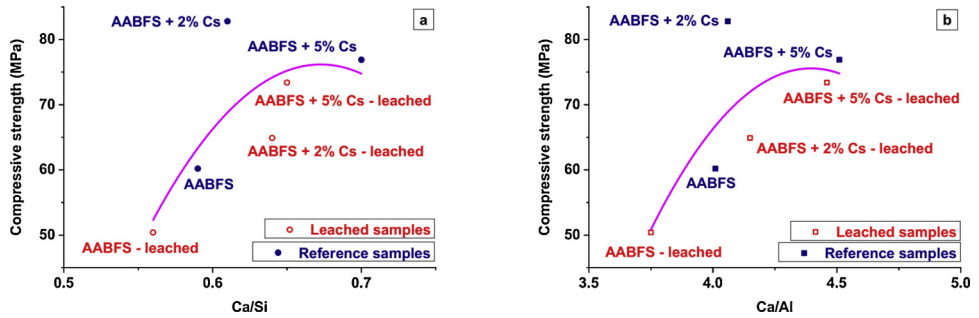

Fig. 9. Compressive strength of AABFS specimens (with and without Cs added; before and after leaching) versus: a) Ca/Si atomic ratio, and b) Ca/Al atomic ratio.

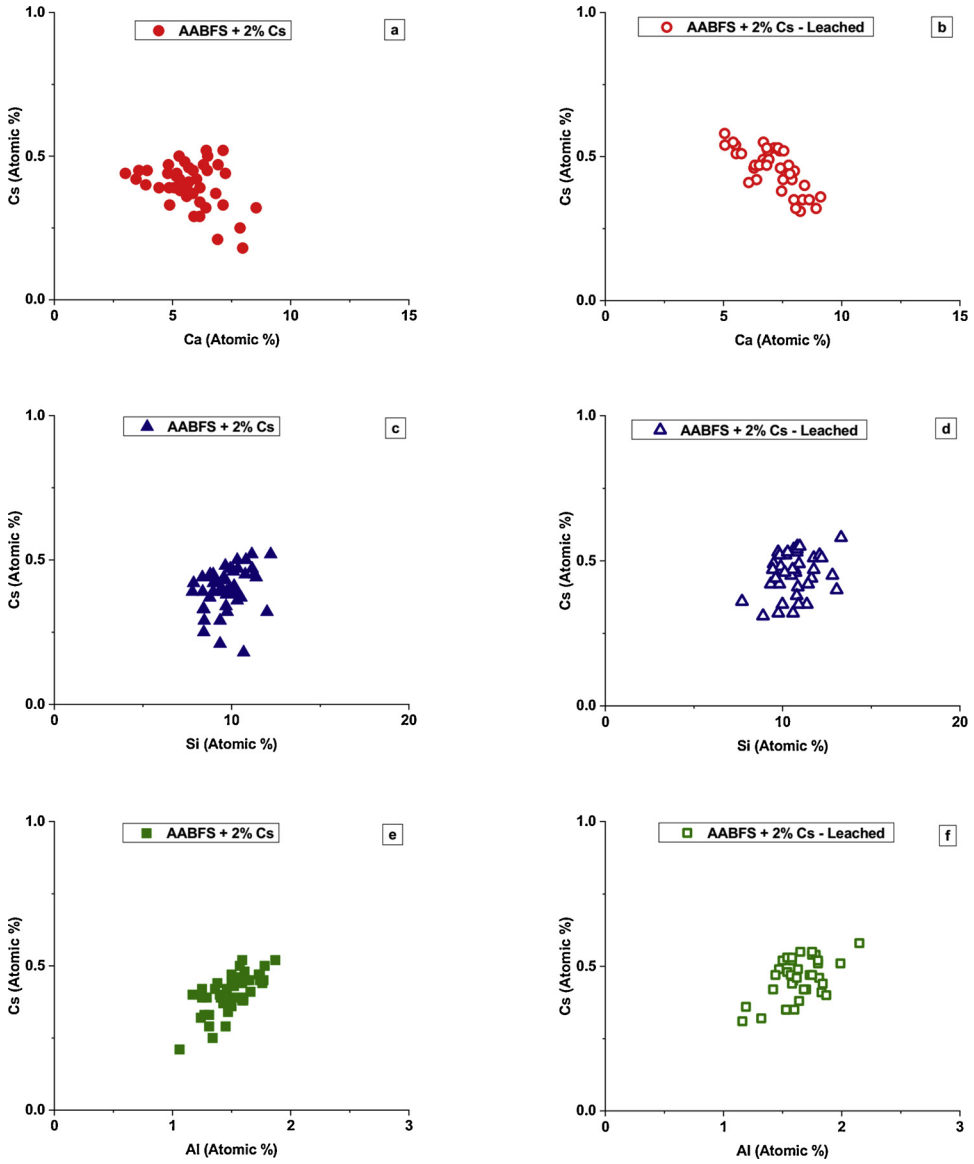

Fig. 10. EDS analysis of AABFS doped with 2 % Cs (before and after leaching).

$$MCL_{(cross\text{-}linked)} = 4[Q^1 + Q^2(0Al) + Q^2(1Al) + Q^3(0Al) + 2Q^3(1Al)]/Q^1 \quad (4)$$

$$Al^{(IV)}/Si = [Q^2(1Al) + Q^3(1Al)]/[Q^1 + Q^2(0Al) + Q^2(1Al) + Q^3(0Al) + 2Q^3(1Al)] \quad (5)$$

The results of ^{29}Si MAS NMR spectral deconvolution showed that the number of Q^1 and $Q^2(0Al)$ sites increased after doping AABFS with Cs, while the number of the $Q^2(1Al)$ sites decreased (Table 7). This led to a decrease in the Al^{IV}/Si ratio of the C-A-S-H gel, with a reduction of the mean chain length (MCL; Fig. 15a).

The significant increase of the AABFS mortar strength when doped with Cs can be connected with the decreased Al/Si ratio (Fig. 15b) and decreased MCL of the C-A-S-H gel (Fig. 15c). The additional alkali cations (2 % or 5 % Cs) present in the AABFS matrix promoted the dissolution and alkali activation of BFS, evident through the reduced amount of remnant BFS ($Q^0_{disordered}$) sites (Table 7). The formation of additional $Q^n(mAl)$ sites (n = 1–3, m = 0–1) present in the C-A-S-H gel is clearly visible in Fig. 15d, while simultaneous formation of $Q^n(mAl)$ sites (n = 4, m = 1–4) due to the doping with Cs is visible in Fig. 15e and Table 7. This is evidence of aluminosilicate (N-A-S-H) gel formation as a result of doping AABFS with Cs; this newly formed gel can probably host some calcium as well, so may be described as N-(C)-A-S-H.

Recently published molecular dynamics simulations (Jiang et al., 2017; Duque-Redondo et al., 2018; Arayro et al., 2018), used to analyze the interaction of cesium and C-S-H gel, did not predict the formation of additional N-(C)-A-S-H gel as a result of C-S-H doping with Cs. Molecular dynamics simulation is a force-field-based nanoscale simulation method and the correctness of molecular dynamics simulations depends on the force field selected and the constraints applied in modelling the gel (Ma et al., 2019). Many molecular dynamics simulations are based on empirical force fields; hence, finding an appropriate force field for molecular dynamics simulations is of utmost importance.

After leaching the Al^{IV}/Si ratio further decreased to zero while the MCL increased (Fig. 15a), which means that the C-A-S-H gel was converted to more cross-linked silica-rich C–S–H gel. This is in agreement with the results of EDS analysis (Fig. 11). Quite a small amount of aluminum was measured in the leachate after leaching (Figs. 1d and 2 d), which is also in agreement with the results obtained by EDS analysis since the Al/Si ratio remained in a very narrow range before and after leaching (Table 6). The proportion of Q^4 sites was very low in the case of AABFS, and also when AABFS was doped with Cs. However, after leaching it was not possible to identify $Q^2(1Al)$ sites in all cases

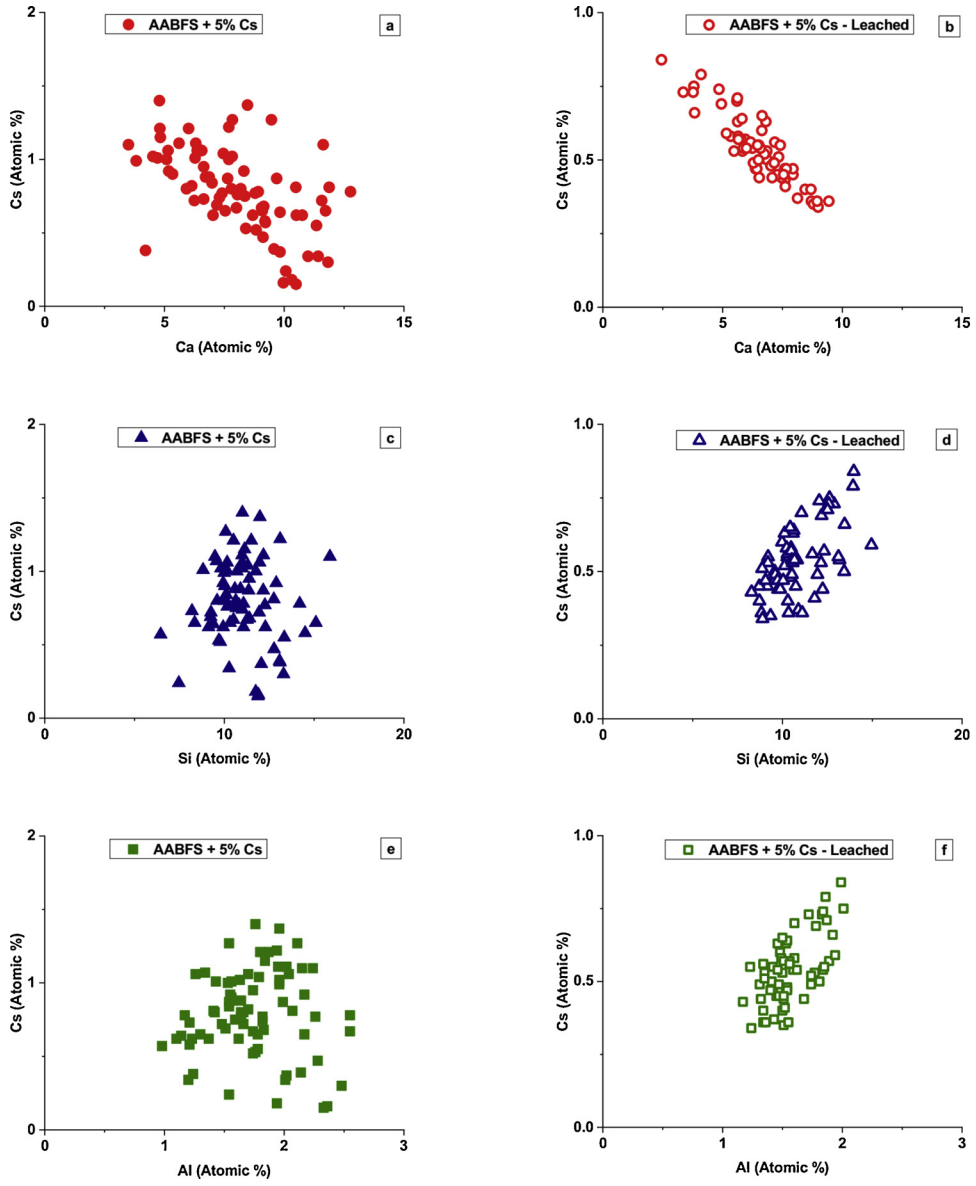

Fig. 11. EDS analysis of AABFS doped with 5 % Cs (before and after leaching).

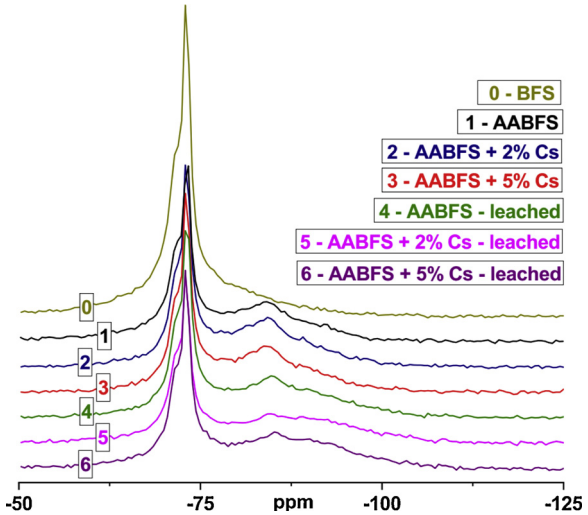

Fig. 12. ^{29}Si MAS-NMR spectra of BFS and AABFS (with and without Cs added, before and after leaching).

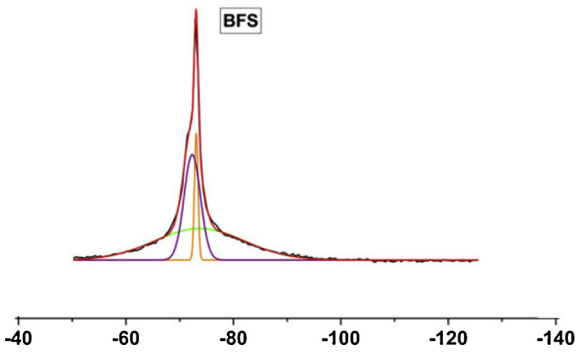

Fig. 13. Deconvolution of the ^{29}Si MAS-NMR spectrum of BFS.

(Table 7); consequently Q^3(1Al) sites also ceased to exist and additional Q^4(mAl) (m = 1–4) sites were formed. This means that the majority of the aluminum that was mobilized due to the breakage of Al-O-Si bonds in the C-A-S-H gel remained in the AABFS matrix, initiating some kind of gel reconstruction - i.e., the C-A-S-H gel was converted to C–S–H gel and additional N-(C)-A-S-H gel was formed. The results given in

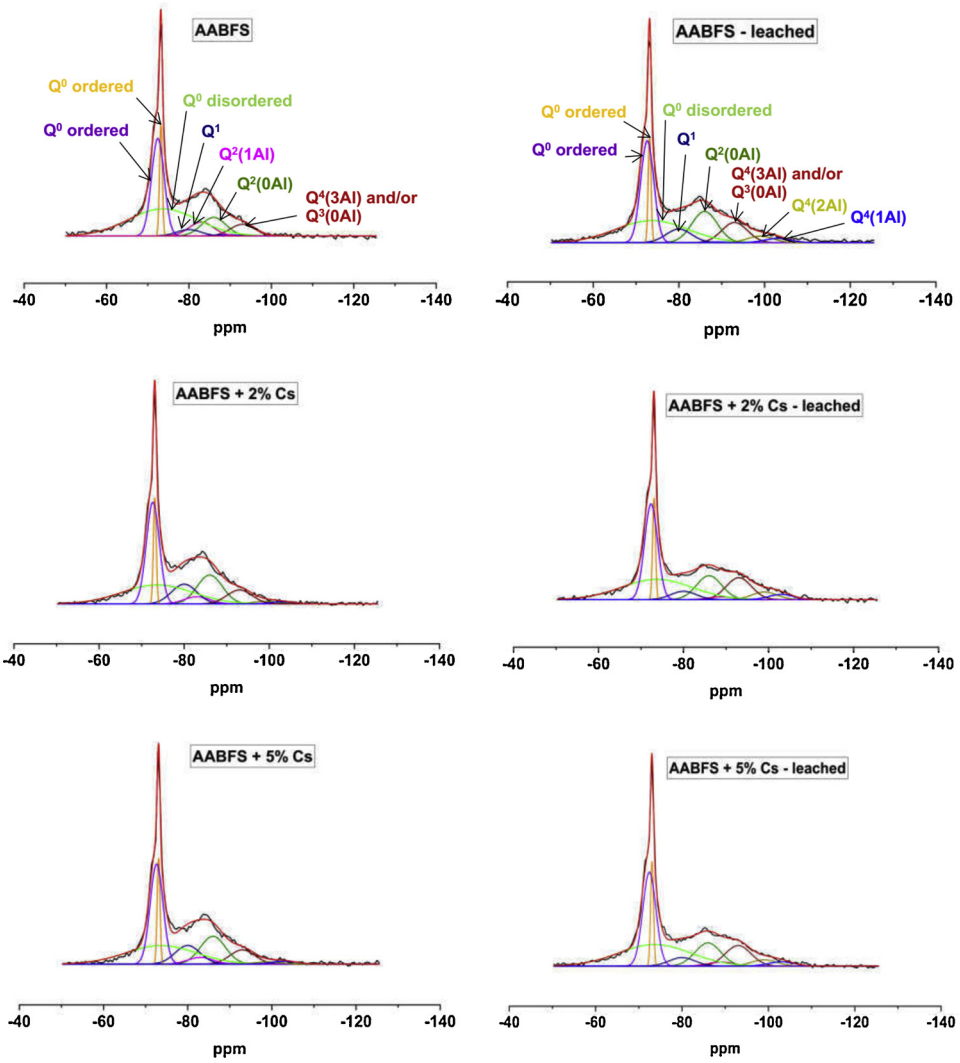

Fig. 14. Deconvolution of ^{29}Si MAS-NMR spectra of AABFS (with and without Cs added, before and after leaching).

Fig. 15e are clear evidence of this nanostructural alteration of AABFS due to leaching. Furthermore, the increase of $Q^0_{disordered}$ (amorphous) sites after leaching might suggest the presence of some isolated silica tetrahedra within the AABFS matrix, as reported previously (Gao et al., 2017).

The reduction of the Al^{IV}/Si ratio and MCL of the C-A-S-H gel caused by leaching resulted in a loss of strength of AABFS mortars (Fig. 15b and c, and Table 5). On the other hand, when AABFS was doped with Cs, the loss of strength was instead connected with the lower amount of C-S-H gel (Fig. 15d) and higher amount of N-(C)-A-S-H gel (Fig. 15e) present in the AABFS matrix. This highlights that there were two competing processes taking place during leaching. The first involved the reduction of the Al/Si ratio and MCL of silicate chains present in the C-A-S-H gel, as well as the decrease of the total amount of Q^n(mAl) sites (n = 1–3, m = 0–1). The second involved the increase of the total amount of Q^n(mAl) sites (n = 4, m = 1–4), i.e., formation of the N-(C)-A-S-H gel, and probably incorporated the majority of Cs when AABFS was doped with it, as suggested by EDS analysis (Figs. 10 and 11).

4. Conclusions

In this paper the mechanical and structural properties of alkali-activated binders (AAB) based on blast furnace slag (BFS), doped with 2 % and 5 % cesium (i.e., a solidified simulated radioactive waste), before

Table 7
Location (ppm) and relative distribution (%) of Q^n(mAl) sites.

Site		Q^0 ordered	Q^0 disordered	Q^1	Q^2(1Al)	Q^2(0Al)	Q^3(1Al) and/or Q^4(4Al)	Q^4(3Al) and/or Q^3(0Al)	Q^4(2Al)	Q^4(1Al)
Location (ppm)		−72.3 −73.1	−73.7	−80.0	−83.0	−86.0	−89.0	−93.0	−99.0	−103.0
Sample	AABFS	33	39	4	6	11	< 0.5	6	0	0
	AABFS + 2 % Cs	34	28	10	4	15	< 0.5	7	1	1
	AABFS + 5 % Cs	34	28	10	4	15	< 0.5	8	1	1
	AABFS - leached	32	30	7	0	15	< 0.5	10	3	2
	AABFS + 2 % Cs - leached	32	30	4	0	13	1	12	4	3
	AABFS + 5 % Cs - leached	32	32	5	0	12	2	11	3	2

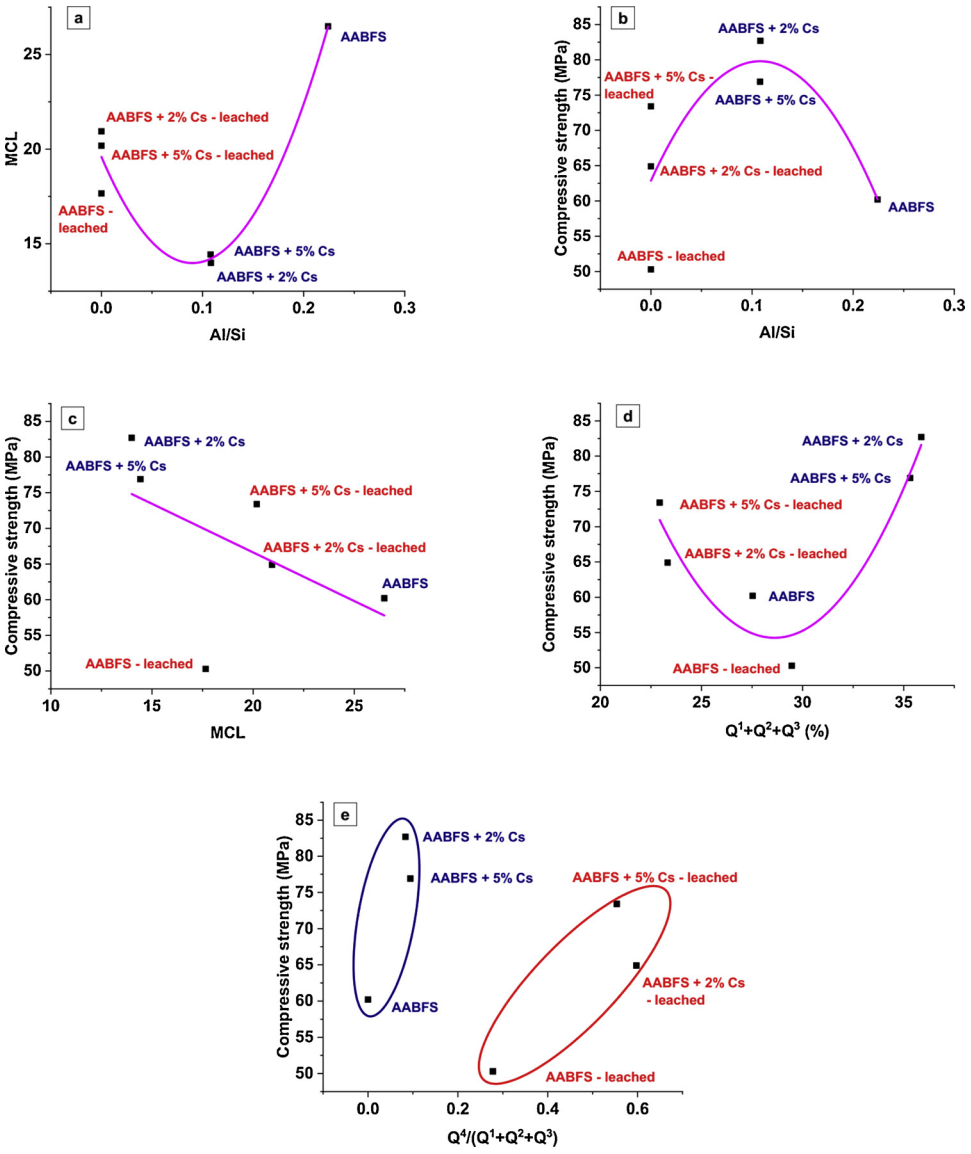

Fig. 15. Different relationships between material characteristics, based on deconvolution of ^{29}Si MAS-NMR spectra of AABFS (with and without Cs added, before and after leaching).

and after leaching according to the ANSI/ANS-16.1-2003standard procedure, were investigated. Based on the results presented, the following conclusions can be drawn:

i) The short (up to 5 days) semi-dynamic process of leaching from AABFS can be divided into two distinct stages: a) fast leaching of non-bound or loosely bound ions in the initial 24 h, which occurred mostly between the surface of AABFS and the leachant, and b) slower leaching in the later stages of the experiment which was controlled by diffusion of ions through the AABFS matrix.
ii) The calculated diffusion coefficients (D) and leachability indexes (L) of cesium suggested that AABFS can be considered as a potentially efficient matrix for cesium immobilization, since the mean leachability index in both cases (2 % and 5 %) was above the threshold value of 6.
iii) The doping of AABFS with Cs had a positive impact on its strength development due to the promotion of dissolution of BFS and structural reorganization of the gels present in AABFS. However, after 5-day leaching tests all of the AABFS mortar samples did show some loss of strength.
iv) Cesium was identified to be preferentially associated with the alkali-aluminosilicate gel (identifiable by NMR spectroscopy and enhanced by the presence of Cs) rather than with the calcium aluminosilicate gel within the AABFS phase assemblage. The results of this research seem to be in good agreement with the cross-linked substituted tobermorite model (CSTM) (Myers et al., 2013) that describes the C-(*N*)-A-S-H gel as a mixture of cross-linked and non-crosslinked tobermorite-based structures, which also included the presence of an additional activation product that contains highly connected four-coordinated silicate and aluminate species.
v) There was a good correlation between the Ca/Si or Ca/Al ratios obtained by SEM/EDS analysis and compressive strength, suggesting that an increase of these ratios is linked to the compressive strength increase when AABFS was doped with Cs, while the situation was reversed after leaching.
vi) Correlations between mortar compressive strength and C-A-S-H gel properties (Al/Si ratio, the mean chain length (MCL), and the total amount of Q^{1-3} sites) were also established.
vii) The majority of the aluminum that was released from the C-A-S-H gel due to the leaching and breakage of Al-O-Si bonds remained within the AABFS matrix, initiating certain gel reconstruction processes: the C-A-S-H gel was converted to

CRediT authorship contribution statement

M. Komljenović: Conceptualization, Methodology, Validation, Formal analysis, Resources, Writing - original draft, Supervision, Project administration, Funding acquisition. **G. Tanasijević:** Investigation, Validation. **N. Džunuzović:** Investigation, Formal analysis. **J.L. Provis:** Conceptualization, Methodology, Validation, Formal analysis, Resources, Writing - original draft, Supervision, Project administration, Funding acquisition.

Declaration of Competing Interest

The authors declare that they have no known competing financial interests or personal relationships that could have appeared to influence the work reported in this paper

Acknowledgements

This research was financially supported by the NATO SPS programme (project G5402) and the Ministry of Education, Science and Technological Development of the Republic of Serbia (project TR 34,026). The authors would like to thank Dr. Ljiljana Kostić-Kravljanac (Institute for Multidisciplinary Research, University of Belgrade) for assistance in acquiring the ICP–OES data, Dr. Marin Tadić (Institute for nuclear sciences, University of Belgrade) for the XRD data, and Dr. Zoran Miladinović (Institute of general and physical chemistry, Belgrade) for the NMR data.

References

Abdel Rahman, R.O., Rakhimov, R.Z., Rakhimova, N.R., Ojovan, M.I., 2015. Cementitious Materials for Nuclear Waste Immobilization. John Wiley Sons Ltd.

Abdel Rahman, R.O., Zaki, A.A., El-Kamash, A.M., 2007. Modeling the long-term leaching behavior of ^{137}Cs, ^{60}Co, and ^{152,154}Eu radionuclides from cement–clay matrices. J. Hazard. Mater. 145, 372–380. https://doi.org/10.1016/j.jhazmat.2006.11.030.

Abdel Rahman, R.O., Zaki, A.A., 2009. Assessment of the leaching characteristics of incineration ashes in cement matrix. Chem. Eng. J. 155, 698–708. https://doi.org/10.1016/j.cej.2009.09.002.

Al-Jubouri, S.M., Curry, N.A., Holmes, S.M., 2016. Hierarchical porous structured zeolite composite for removal of ionic contaminants from waste streams and effective encapsulation of hazardous waste. J. Hazard. Mater. 320, 241–251. https://doi.org/10.1016/j.jhazmat.2016.08.011.

ANSI/ANS-16.1–2003 (R2017), Measurement of the leachability of solidified low-level radioactive wastes by a short-term test procedure, American Nuclear Society.

Arayro, J., Dufresne, A., Zhou, T., Ioannidou, K., Ulm, J.-F., Pellenq, R., Béland, L.K., 2018. Thermodynamics, kinetics, and mechanics of cesium sorption in cement paste: a multiscale assessment. Phys. Rev. Mater. 2 (053608), 1–10. https://doi.org/10.1103/PhysRevMaterials.2.053608.

Arbel Haddad, M., Ofer-Rozovsky, E., Bar-Nes, G., Borojovich, E.J.C., Nikolski, A., Mogiliansky, D., Katz, A., 2017. Formation of zeolites in metakaolin-based geopolymers and their potential application for Cs immobilization. J. Nucl. Mater. 493, 168–179. https://doi.org/10.1016/j.jnucmat.2017.05.046.

Bernal, S.A., Krivenko, P.V., Provis, J.L., Puertas, F., Rickard, W.D.A., Shi, C., van Riessen, A., 2014. Other potential applications for alkali-activated materials. Chapter 12 In: Provis, J.L., van Deventer, J.S.J. (Eds.), Alkali Activated Materials: State-of-the-Art Report, RILEM TC 224-AAM. RILEM, pp. 339–381.

Bernal, S.A., de Gutierrez, R.M., Provis, J.L., Rose, V., 2010. Effect of silicate modulus and metakaolin incorporation on the carbonation of alkali silicate-activated slags. Cem. Concr. Res. 40, 898–907. https://doi.org/10.1016/j.cemconres.2010.02.003.

Bernal, S.A., Provis, J.L., Walkley, B., San Nicolas, R., Gehman, J.D., Brice, D.G., Kilcullen, A.R., Duxson, P., van Deventer, J.S.J., 2013. Gel nanostructure in alkali-activated binders based on slag and fly ash, and effects of accelerated carbonation. Cem. Concr. Res. 53, 127–144. https://doi.org/10.1016/j.cemconres.2013.06.007.

Cantarel, V., Nouaille, F., Rooses, A., Lambertin, D., Poulesquen, A., Frizon, F., 2015. Solidification/stabilisation of liquid oil waste in metakaolin-based geopolymer. J. Nucl. Mater. 464, 16–19. https://doi.org/10.1016/j.jnucmat.2015.04.036.

Chen, J.J., Thomas, J.J., Taylor, H.F.W., Jennings, H.M., 2004. Solubility and structure of calcium silicate hydrate. Cem. Concr. Res. 34, 1499–1519. https://doi.org/10.1016/j.cemconres.2004.04.034.

Deng, N., An, H., Cui, H., Pan, Y., Wang, B., Mao, L., Zhai, J., 2015. Effects of gamma-ray irradiation on leaching of simulated $^{133}Cs^{+}$ radionuclides from geopolymer wasteforms. J. Nucl. Mater. 459, 270–275. https://doi.org/10.1016/j.jnucmat.2015.01.052.

Duque-Redondo, E., Kazuo, Y., López-Arbeloa, I., Manzano, H., 2018. Cs-137 immobilization in C-S-H gel nanopores. J. Chem. Soc. Faraday Trans. 20, 9289–9297. https://doi.org/10.1039/c8cp00654g.

El-Naggar, M.R., 2014. Applicability of alkali activated slag-seeded Egyptian Sinai kaolin for the immobilization of ^{60}Co radionuclide. J. Nucl. Mater. 447, 15–21. https://doi.org/10.1016/j.jnucmat.2018.02.023.

El-Naggar, M.R., Amin, M., 2018. Impact of alkali cations on properties of metakaolin and metakaolin/slag geopolymers: microstructures in relation to sorption of ^{134}Cs radionuclide. J. Hazard. Mater. 344, 913–924. https://doi.org/10.1016/j.jhazmat.2017.11.049.

El-Naggar, M.R., El-Masry, E.H., El-Sadek, A.A., 2019. Assessment of individual and mixed alkali activated binders for solidification of a nuclear grade organic resin loaded with ^{134}Cs, ^{60}Co and $^{152+154}$Eu radionuclides. J. Hazard. Mater. 375, 149–160. https://doi.org/10.1016/j.jhazmat.2019.04.063.

EN 1015-3: 2008, Methods of test for mortar for masonry - Part 3: Determination of consistence of fresh mortar (by flow table).

EN 196-1: 2008, Methods of testing cement – part 1: determination of strength.

EN 196–3: 2008, Methods of testing cement Part 3: Determination of setting times and soundness.

Gao, X., Yu, Q.L., Brouwers, H.J.H., 2017. Apply ^{29}Si, ^{27}Al MAS NMR and selective dissolution in identifying the reaction degree of alkali activated slag-fly ash composites. Ceram. Int. 43, 12408–12419. https://doi.org/10.1016/j.ceramint.2017.06.108.

García Lodeiro, I., Fernández-Jiménez, A., Teresa Blanco, M., Palomo, A., 2008. FTIR study of the sol–gel synthesis of cementitious gels: C–S–H and N–a–S–H. J. Solgel Sci. Technol. 45, 63–72. https://doi.org/10.1007/s10971-007-1643-6.

García Lodeiro, I., Macphee, D.E., Palomo, A., Fernández-Jiménez, A., 2009. Effect of alkalis on fresh C–S–H gels. FTIR analysis, Cement and Concrete Research 39, 147–153. https://doi.org/10.1016/j.cemconres.2009.01.003.

Glasser, F., 2011. Application of inorganic cements to the conditioning and immobilisation of radioactive wastes. In: Ojovan, M.I. (Ed.), Handbook of Advanced Radioactive Waste Conditioning Technologies. Woodhead Publishing, pp. 67–135.

Jang, J.G., Park, S.M., Lee, H.K., 2016. Physical barrier effect of geopolymeric waste form on diffusivity of cesium and strontium. J. Hazard. Mater. 318, 339–346. https://doi.org/10.1016/j.jhazmat.2016.07.003.

Jiang, J., Wang, P., Hou, D., 2017. The mechanism of cesium ions immobilization in the nanometer channel of calcium silicate hydrate: a molecular dynamics study. J. Chem. Soc. Faraday Trans. 19, 27974–27986. https://doi.org/10.1039/c7cp05437h.

Komljenović, M., 2015. Mechanical strength and Young's modulus of alkali activated cement-based binders. Chapter 7 In: Pacheco-Torgal, F., Labrincha, J.A., Leonelli, C., Palomo, A., Chindaprasirt, P. (Eds.), Handbook of Alkali-Activated Cements, Mortars and Concretes, Woodhead Publishing Series in Civil and Structural Engineering, pp. 171–217.

Komljenovic, M., Bascarevic, Z., Bradic, V., 2010. Mechanical and microstructural properties of alkali-activated fly ash geopolymers. J. Hazard. Mater. 181, 35–42. https://doi.org/10.1016/j.jhazmat.2010.04.064.

Komljenović, M., Baščarević, Z., Marjanović, N., Nikolić, V., 2012. Decalcification resistance of alkali-activated slag. J. Hazard. Mater. 233–234, 112–121. https://doi.org/10.1016/j.jhazmat.2012.06.063.

Kryvenko, P., Cao, H., Petropavlovskyi, O., Weng, L., Kovalchuk, O., 2015. Applicability of alkali-activated cement for immobilization of low-level radioactive waste in ion-exchange resins. East. J. Enterp. Technol. 79, 40–45. https://doi.org/10.15587/1729-4061.2016.59489.

Kuenzel, C., Cisneros, J.F., Neville, T.P., Vandeperre, L., Simons, S.J.R., Bensted, J., Cheeseman, C.R., 2015. Encapsulation of Cs/Sr contaminated clinoptilolite geopolymers produced from metakaolin. J. Nucl. Mater. 466, 94–99. https://doi.org/10.1016/j.jnucmat.2015.07.034.

Lambertin, D., Boher, C., Dannoux-Papin, A., Galliez, K., Rooses, A., Frizon, F., 2013. Influence of gamma ray irradiation on metakaolin based sodium geopolymer. J. Nucl. Mater. 443, 311–315. https://doi.org/10.1016/j.jnucmat.2013.06.044.

Lancellotti, I., Barbieri, I., Leonelli, C., 2015. Use of alkali-activated concrete binders for toxic waste immobilization. Chapter 20 In: Labrincha, J.A., Leonelli, C., Palomo, A., Chindaprasirt, P. (Eds.), Handbook of Alkali-Activated Cements, Mortars and Concretes, F. Pacheco-Torgal. Woodhead Pher Potential Applications for Alkali-Activated Materia publishing, pp. 539–604.

Li, Q., Sun, Z., Tao, D., Xu, Y., Li, P., Cui, H., Zhai, J., 2013. Immobilization of simulated radionuclide $^{133}Cs^{+}$ by fly ash-based geopolymer. J. Hazard. Mater. 262, 325–331. https://doi.org/10.1016/j.jhazmat.2013.08.049.

Ma, Zhaoyang, Gamage, Ranjith Pathegama, Rathnaweera, Tharaka, Kong, Lie, 2019. Review of application of molecular dynamic simulations in geological highlevel radioactive waste disposal. Appl. Clay Sci. 168, 436–449. https://doi.org/10.1016/j.clay.2018.11.018.

Marjanović, N., Komljenović, M., Baščarević, Z., Nikolić, V., Petrović, R., 2015. Physical–mechanical and microstructural properties of alkali-activated fly ash–blast furnace slag blends. Ceram. Int. 41, 1421–1435. https://doi.org/10.1016/j.ceramint.2014.09.075.

Myers, R.J., Bernal, S.A., San Nicolas, R., Provis, J.L., 2013. Generalized structural description of calcium-sodium aluminosilicate hydrate gels: the cross-linked substituted tobermorite model. Langmuir 29, 5294–5306. https://doi.org/10.1021/la4000473.

Myers, R.J., Bernal, S.A., Provis, J.L., 2017. Phase diagrams for alkali-activated slag binders. Cem. Concr. Res. 95, 30–38. https://doi.org/10.1016/j.cemconres.2017.02.006.

Myers, R.J., Bernal, S.A., Gehman, J.D., van Deventer, J.S.J., Provis, J.L., 2015. The role of Al in cross-linking of alkali-activated slag cements. J. Am. Ceram. Soc. 98 (3), 996–1004. https://doi.org/10.1111/jace.13360.

Nedeljkovic, M., Zuo, Y., Arbi, K., Ye, G., 2018. Carbonation resistance of alkali-activated slag under natural and accelerated conditions. J. Sustain. Metall. 4, 33–49. https://doi.org/10.1007/s40831-018-0166-4.

Nikolić, V., Komljenović, M., Baščarević, Z., Marjanović, N., Miladinović, Z., Petrović, R., 2015. The influence of fly ash characteristics and reaction conditions on strength and

structure of geopolymers. Constr. Build. Mater. 94, 361–370. https://doi.org/10.1016/j.conbuildmat.2015.07.014.
Nikolić, V., Komljenović, M., Džunuzović, N., Miladinović, Z., 2018. The influence of Pb addition on the properties of fly ash-based geopolymers. J. Hazard. Mater. 350, 98–107. https://doi.org/10.1016/j.jhazmat.2018.02.023.
Pacheco-Torgal, F., Labrincha, J.A., Leonelli, C., Palomo, A., Chindaprasirt, P. (Eds.), 2015. Handbook of Alkali-Activated Cements, Mortars and Concretes. Woodhead Publishing Series in Civil and Structural Engineering.
Palacios, M., Puertas, F., 2011. Effectiveness of mixing time on hardened properties of waterglass-activated slag pastes and mortars. Aci Mater. J. 108 (1), 73–78.
Palacios, M., Puertas, F., 2006. Effect of carbonation on alkali-activated slag paste. J. Am. Ceram. Soc. 89, 3211–3221. https://doi.org/10.1111/j.1551-2916.2006.01214.x.
Palomo, A., Blanco-Varela, M.T., Granizo, M.L., Puertas, F., Vazquez, T., Grutzeck, M.W., 1999. Chemical stability of cementitious materials based on metakaolin. Cem. Concr. Res. 29, 997–1004.
Provis, J.L., Palomo, A., Shi, C., 2015. Advances in understanding alkali-activated materials. Cem. Concr. Res. 78, 110–125. https://doi.org/10.1016/j.cemconres.2015.04.013.
Provis, J.L., van Deventer, J.S.J. (Eds.), 2014. Alkali-Activated Materials: State-of-the-Art Report, RILEM TC 224-AAM. Springer/RILEM, Dordrecht.
Salis, A., Ninham, B.W., 2014. Models and mechanisms of Hofmeister effects in electrolyte solutions, and colloid and protein systems revisited. Chem. Soc. Rev. 43, 7358–7377. https://doi.org/10.1039/c4cs00144c.
Shi, C., Qu, B., Provis, J.L., 2019. Recent progress in low-carbon binders. Cem. Concr. Res. 122, 227–250. https://doi.org/10.1016/j.cemconres.2019.05.009.
Steins, P., Poulesquen, A., Diat, O., Frizon, F., 2012. Structural evolution during geopolymerization from an early age to consolidated material. Langmuir 28, 8502–8510. https://doi.org/10.1021/la300868v.
Tsutsumi, T., Nishimoto, S., Kameshima, Y., Miyake, M., 2014. Hydrothermal preparation of tobermorite from blast furnace slag for Cs^{+} and Sr^{2+} sorption. J. Hazard. Mater. 266, 174–181. https://doi.org/10.1016/j.jhazmat.2013.12.024.
Vandevenne, N., Iacobescu, R.I., Pontikes, Y., Carleer, R., Thijssen, E., Gijbels, K., Schreurs, S., Schroeyers, W., 2018. Incorporating Cs and Sr into blast furnace slag inorganic polymers and their effect on matrix properties. J. Nucl. Mater. 503, 1–12. https://doi.org/10.1016/j.jnucmat.2018.02.023.
Wagh, A.S., Sayenko, S.Y., Shkuropatenko, V.A., Tarasov, R.V., Dykiy, M.P., Svitlychniy, Y.O., Virych, V.D., Ulybkina, E.A., 2016. Experimental study on cesium immobilization in struvite structures. J. Hazard. Mater. 302, 241–249. https://doi.org/10.1016/j.jhazmat.2015.09.049.
Walkley, B., Provis, J.L., 2019. Solid-state nuclear magnetic resonance spectroscopy of cements. Materials Today Advances 1, 100007. https://doi.org/10.1016/j.mtadv.2019.100007.
Walkley, Brant, Ke, Xinyuan, Hussein, Oday H., Bernal, Susan A., Provis, John L., 2020. Incorporation of strontium and calcium in geopolymer gels. J. Hazard. Mater. 382https://doi.org/10.1016/j.jhazmat.2019.121015. 121015.
Wang, Lei, Chen, Liang, Cho, Dong-Wan, Tsang, Daniel C.W., Yang, Jian, Hou, Deyi, Baek, Kitae, Kua, Harn Wei, Poon, Chi-Sun, 2019. Novel synergy of Si-rich minerals and reactive MgO for stabilisation/solidification of contaminated sediment. J. Hazard. Mater. 365, 695–706. https://doi.org/10.1016/j.jhazmat.2018.11.067.